

# Magneto-toroidal nonreciprocity of second harmonic generation

J. Mund,<sup>1</sup> D. R. Yakovlev,<sup>1,2</sup> A. N. Poddubny,<sup>2</sup> R. M. Dubrovin,<sup>2</sup> M. Bayer,<sup>1,2</sup> and R. V. Pisarev<sup>2,\*</sup>

<sup>1</sup>*Experimentelle Physik 2, Technische Universität Dortmund, D-44221 Dortmund, Germany*

<sup>2</sup>*Ioffe Institute, Russian Academy of Sciences, 194021 St.-Petersburg, Russia*

(Dated: May 13, 2020)

The Lorentz reciprocity principle is a fundamental concept that governs light propagation in any optically linear medium in zero magnetic field. Here, we demonstrate experimentally a novel mechanism of reciprocity breaking in nonlinear optics driven by the toroidal moment. Using high-resolution femtosecond spectroscopy at optical electronic resonances in the magnetoelectric antiferromagnet  $\text{CuB}_2\text{O}_4$ , we show that by controlling the nonlinear interference of coherent sources of second harmonic generation originating from the toroidal spin order, applied magnetic field, and noncentrosymmetric crystal structure, we induce a huge nonreciprocity approaching 100% for opposite magnetic fields. The experimental results are corroborated by a convincing theoretical analysis based on the magnetic and crystal symmetry. These findings open new degrees of freedom in the nonlinear physics of electronic and magnetic structures and pave the way for future nonreciprocal spin-optronic devices operating on the femtosecond time scale.

A magnetic field induces optical nonreciprocity in any linear medium enabling one-way routing of light [1–3], which can be revealed by studying the Faraday rotation or magnetic circular dichroism, as sketched in Fig. 1a. In nonlinear optics, the time-reversal symmetry is inherently broken and the principle of reciprocity is not valid even in the absence of a magnetic field [4–6]. Nonlinear nonreciprocal effects become especially rich when complemented by the breaking of spatial inversion symmetry and nontrivial spin order [7–12]. Despite rapid recent progress [13–15], this field has remained mostly uncharted so that novel, non-trivial effects from nonlinear and nonreciprocal resonant light-matter interactions due to the coupling of charge, orbital and spin degrees of freedom can be expected.

Here, we demonstrate widely tunable nonlinear reciprocity breaking due to interference of symmetry-different optical second harmonic generation (SHG) sources induced by an applied magnetic field  $\mathbf{B}$  and a toroidal moment  $\mathbf{T}$ , as shown schematically in Fig. 1b. The toroidal order, initially introduced in high-energy physics [16], currently attracts tremendous attention across disciplines ranging from spin physics of multiferroics and magnetoelectrics [6, 8, 13, 17–22] to nanoscale optics [23]. However, the giant nonlinear magneto-toroidal nonreciprocity discovered here through the contribution

$$|E^{2\omega}(\mathbf{B})|^2 - |E^{2\omega}(-\mathbf{B})|^2 \propto B_x T_x |E_z^\omega|^4 \quad (1)$$

to the SHG intensity, has never been reported before to the best of our knowledge. Our findings are based on high-sensitivity and high-resolution femtosecond spectroscopy of resonant optical SHG from the antiferromagnetic copper metaborate  $\text{CuB}_2\text{O}_4$  and corroborated by a rigorous symmetry analysis.

The choice of  $\text{CuB}_2\text{O}_4$  is motivated by its favorable combination of exceptionally narrow optical resonances and magnetic phase diagrams with different types of spin ordering. This opens up yet unexplored opportunities for disclosing new mechanisms of nonlinear nonreciprocity. We focus on the SHG at the electronic resonance near 1.405 eV (Fig. 1c), taking place between the  $3d^9$  states of the  $\text{Cu}^{2+}$  ions at the  $4b$  Wyckoff positions [24]. While SHG at this transition was observed before [25], it has so far not been studied with respect to SHG nonreciprocity and the underlying mechanisms.

Here we focus on the nonreciprocity due to the coupling between the spins  $S = 1/2$  of the  $\text{Cu}^{2+}$  ions that provide a rich variety of commensurate and incommensurate spin structures [26]. The nonvanishing antiferromagnetic  $\mathbf{L} = \mathbf{S}_1 - \mathbf{S}_2$  and ferromagnetic  $\mathbf{M} = \mathbf{S}_1 + \mathbf{S}_2$  order parameters (Fig. 1b) characterize the commensurate phases. Remarkably, the order parameter  $\mathbf{L}$  not only characterizes the commensurate phases but carry also a nonzero toroidal vector  $\mathbf{T} \propto L_x \hat{\mathbf{y}} + L_y \hat{\mathbf{x}}$ . It is the interference of the SHG activated by the toroidal moment  $\mathbf{T}$  and the SHG induced by the magnetic field  $\mathbf{B}$ , that drives the strong magneto-toroidal SHG nonreciprocity according to Eq. (1). We achieve full control of sign and magnitude of this nonreciprocity by changing the direction and magnitude of the magnetic field. Additional nonreciprocity pathways are offered by the spectrally-broad crystallographic SHG source due to the noncentrosymmetric crystal structure. Its controlled involvement provides SHG spectra containing pronounced Fano-resonances with strong spectral asymmetry as the hallmark of nonlinear interference. Obviously, the interference of SHG sources, illustrated in Fig. 1(c), is not limited to  $\text{CuB}_2\text{O}_4$ , but can be used as new concept for magnetic routing of the nonlinear on- and off-resonant coherent emission in complex media.

\* pisarev@mail.ioffe.ru

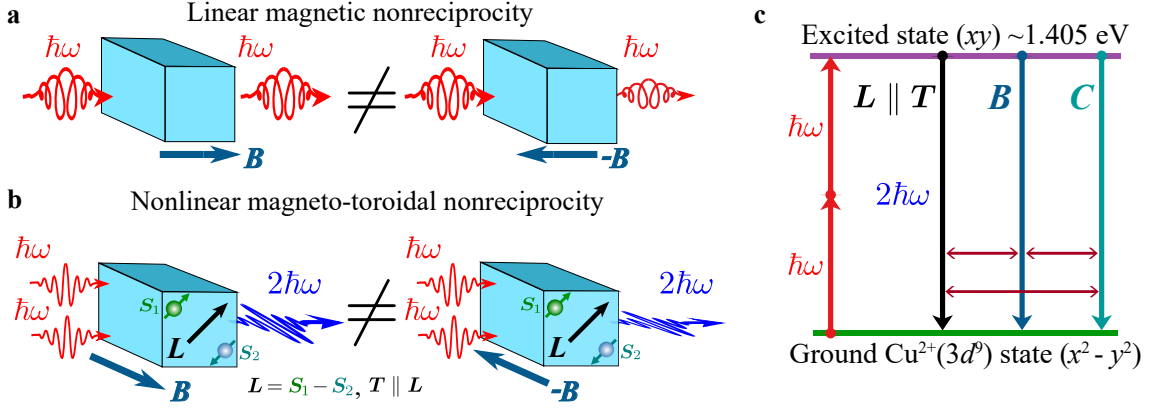


FIG. 1. **Nonreciprocal second harmonic generation in  $\text{CuB}_2\text{O}_4$ .** **a.** Nonreciprocity of light in a linear medium due to different absorption for propagation along or opposite to the applied magnetic field (magnetic circular dichroism). **b.** Nonreciprocal second harmonic generation induced by the magnetic field  $\mathbf{B}$  and the antiferromagnetic moment  $\mathbf{L} = \mathbf{S}_1 - \mathbf{S}_2$  that is parallel to the toroidal moment  $\mathbf{T}$ . **c.** Electronic transition between the ground ( $x^2 - y^2$ ) state and lowest excited ( $xy$ ) state of  $\text{Cu}^{2+}$   $4b$  ions near 1.405 eV [25]. These states are subject to Davydov splitting (not shown) due to the presence of two  $\text{Cu}^{2+}$  ions at  $4b$  sites in the primitive unit cell [27]. The SHG process converts two photons with frequency  $\omega$  into one photon at frequency  $2\omega$ . The vertical lines in Fig. 1c mark the crystallographic ( $C$ ), magnetic-field-induced ( $B$ ), and toroidal ( $T \parallel L$ ) SHG sources. Interference pathways between these sources are indicated by the horizontal double-arrow lines.

## NONLINEAR MAGNETO-TOROIDAL NONRECIPROCALITY

We now present experimental results for the SHG nonreciprocity in two experimental geometries, differing by the applied magnetic field orientation  $\mathbf{B}$  and the resulting antiferromagnetic spin phase.

### Voigt geometry $\mathbf{B} \parallel x, \mathbf{k} \parallel y$

Figure 2 shows SHG spectra in the Voigt geometry when  $\mathbf{B} \parallel x$  and the light wave vector  $\mathbf{k} \parallel y$  (Fig. 2a). The SHG spectra in Fig. 2d are recorded at  $T = 4.0$  K in magnetic fields of  $\pm 8$  T when the antiferromagnetic structure is in the commensurate phase (see phase diagram in Fig. 3a). The spectra can be divided into two groups of sharp lines at 1.4047–1.4049 and 1.4062–1.4063 eV with narrow full widths at half maximum (FWHM) below  $100 \mu\text{eV}$ . We note that no line splitting could be observed in previous studies of  $\text{CuB}_2\text{O}_4$  when the SHG was excited by nanosecond pulses [25]. The observed sharp SHG lines demonstrate the advantages of the femtosecond-pulse technique combined with high spectral resolution (see Methods). The two groups are separated by the Zeeman splitting of about 1.5 meV. Each group demonstrates a small splitting which we assign to the Davydov splitting [27]. The detailed magnetic field dependence of the SHG spectra from 0 to  $\pm 10$  T is discussed in the Supplementary Section S4.

The main result illustrated in Fig. 2d is the strong difference between the SHG spectra for oppositely oriented magnetic fields, compare black and red spectra. This difference gives unambiguous evidence of strong SHG

nonreciprocity, whose degree varies for the different lines and approaches 100% at some photon energies, e.g., for the 1.4062 eV line. With increasing temperature up to  $T = 12.5$  K (Fig. 2e) the SHG lines broaden, but the splitting into two groups and the nonreciprocity remain well pronounced, .

The SHG nonreciprocity is further confirmed by the rotational anisotropies for the  $\mathbf{E}^\omega \perp \mathbf{E}^{2\omega}$  (magenta symbols) and  $\mathbf{E}^\omega \parallel \mathbf{E}^{2\omega}$  (blue symbols) polarization configurations at the 1.4047 and 1.4062 eV lines ( $T = 4.0$  K) in Fig. 2f and the 1.4048 and 1.4059 eV lines ( $T = 12.5$  K) in Fig. 2g. Both series of measurements were performed with the magnetic field  $B = \pm 8$  T, the observed differences can be explained by the difference in the field  $\mathbf{B} \parallel x$  effect on the rearrangement of the antiferromagnetic spins in the ( $xy$ ) plane. In zero field, the antiferromagnetic  $\mathbf{L}$  vector is directed along the easy [110] axis which is the diagonal between the  $x$  and  $y$  axes. But as the  $B_x$  field increases, the  $\mathbf{L}$  vector gradually rotates toward the  $y$  axis perpendicular to the field direction. This process is controlled by sample temperature and magnetic-field strength [28].

The observed nonreciprocity is explained by Eq. (1), describing the interference of the two SHG sources due to the applied magnetic field,  $E_x^{2\omega} \propto (E_z^\omega)^2 B_x$  and the toroidal moment  $\mathbf{T}$ ,  $E_x^{2\omega} \propto (E_z^\omega)^2 \mathbf{T}$ , see Fig. 2(b,c). The toroidal vector, defined for a localized spin distribution as  $\mathbf{T} = \frac{1}{2} \sum_j \mathbf{r}_j \times \mathbf{S}_j$ , in  $\text{CuB}_2\text{O}_4$  is proportional to  $L_y \hat{x} + L_x \hat{y}$ . It is aligned with the [110] axis, similar to the antiferromagnetic moment  $\mathbf{L}$  in the absence of a magnetic field, as shown in Fig. 2c. More formally, the observed SHG is due to the nonlinear magnetoelectric susceptibility  $C_{xzy}^L = C_{yzzx}^L$ , and nonlinear magnetic-field-induced susceptibility  $C_{xxx}^B = -C_{yzyy}^B$ , while the

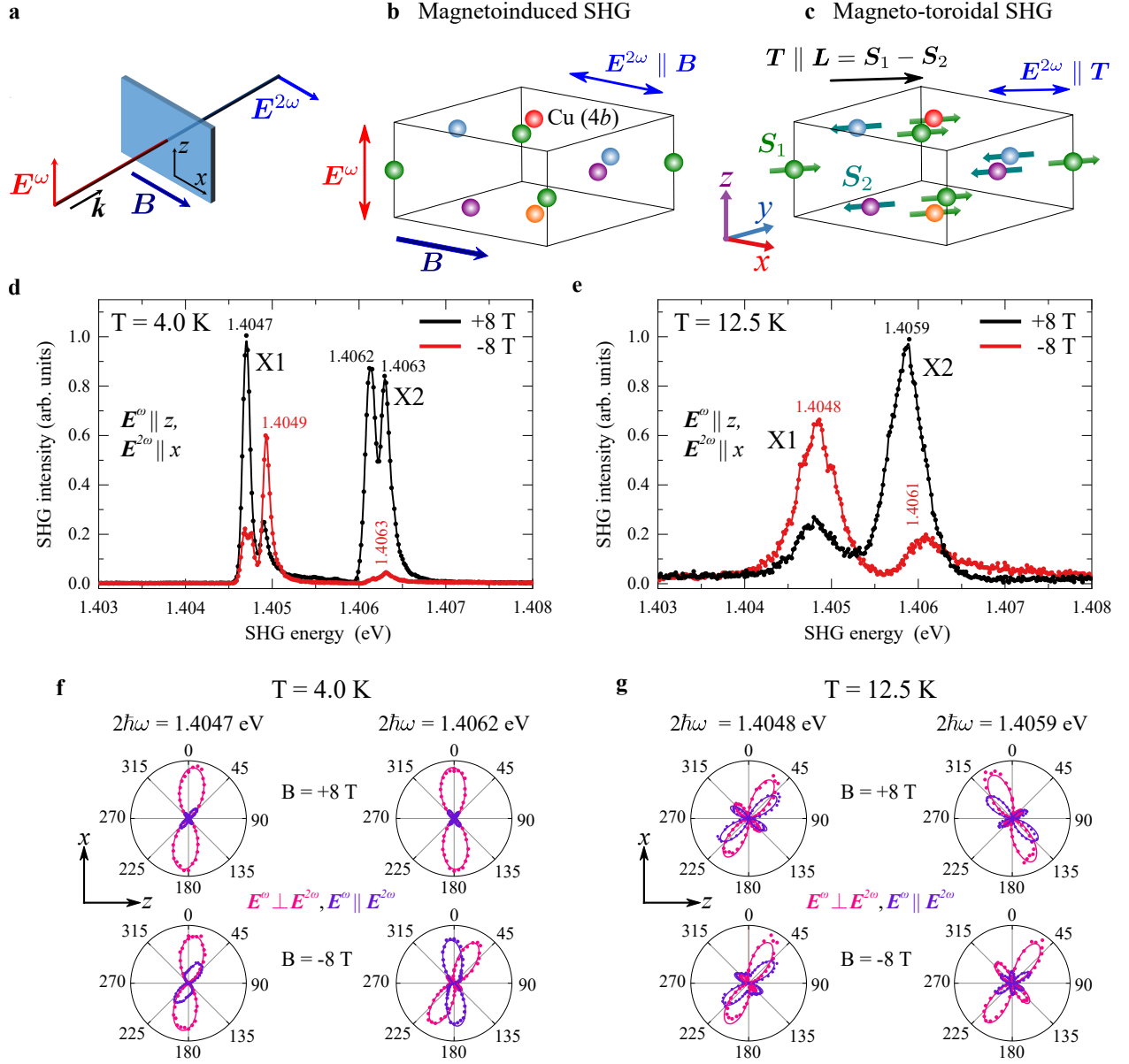


FIG. 2. **Nonreciprocal SHG spectra of  $\text{CuB}_2\text{O}_4$  measured at normal incidence.** **a.** Geometry of the experiment,  $\mathbf{k} \parallel y$  and  $\mathbf{B} \parallel x$ . **b,c.** Polarization  $E^{2\omega}$  of the SHG with respect to the crystal unit cell, induced by the magnetic field (**b**) and by the toroidal moment  $\mathbf{T} \parallel \mathbf{L}$  (**c**). Only  $\text{Cu}^{2+}$  ions at the  $4b$  positions and their spins are shown; ions of the same color have the same  $z$  coordinate. **d.** SHG spectra at  $T = 4.0$  K for opposite fields which demonstrate strong spectral nonreciprocity reaching almost 100% at some lines, e.g., at 1.4062 eV line. **e.** SHG spectra at  $T = 12.5$  K measured in the same geometry as in Fig. 2d. Temperature increase from  $T = 4.0$  to 12.5 K leads to line broadening, drop of the SHG intensity by about an order of magnitude (see Figs. 3b and 3c) but the spectral nonreciprocity remains well pronounced. **f.** Rotational anisotropies at  $T = 4.0$  K for opposite field directions in  $E^\omega \perp E^{2\omega}$  (magenta symbols) and  $E^\omega \parallel E^{2\omega}$  (blue symbols) for the two SHG lines at 1.4047 and 1.4062 eV. These anisotropies are different for opposite fields demonstrating another side of nonreciprocity. **g.** The same as in **f** but at  $T = 12.5$  K for the two SHG peaks at 1.4048 and 1.4059 eV. These rotational anisotropy diagrams are noticeably different from those at  $T = 4.0$  K shown in Fig. 2f. We note that rotational diagrams for opposite fields at  $T = 4.0$  and 12.5 K are similar for the first group of lines but very different for the second group. All rotational diagrams were fitted using equations based on the relevant SHG tensor components given in the Supplementary Section S3.

crystallographic SHG vanishes in the considered geometry. Details of our symmetry analysis are given in the Supplementary Section S2.

The magnetic phase diagram in Fig. 3a shows that

orientation of the antiferromagnetic vector  $\mathbf{L}$  and the toroidal moment  $\mathbf{T}$  is very sensitive to the direction and magnitude of the applied magnetic field. According to Eq. (1), changes of the magnetic structure in the applied

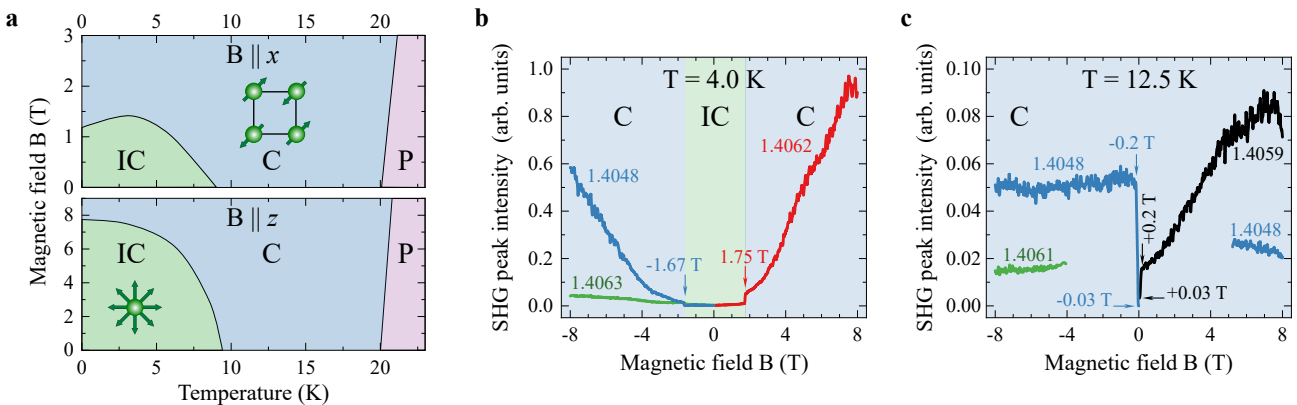


FIG. 3. **Magnetic field dependences of SHG lines originating from the electronic transitions in the vicinity of 1.405 eV in  $\text{CuB}_2\text{O}_4$ .** **a.** Schematic magnetic phase diagrams with the field  $\mathbf{B} \parallel x$  and  $\mathbf{B} \parallel z$ . The designations IC, C, and P refer to the incommensurate, commensurate, and paramagnetic phases. More details related to the phase diagrams can be found in [25, 26, 28–32]. **b.** At  $T = 4.0$  K, no SHG signals are observed for the magnetic field in the range  $-1.67 < B < 1.75$  T when  $\text{CuB}_2\text{O}_4$  is in the incommensurate phase. Outside this field range, SHG lines appear and their field dependences are different for opposite field directions evidencing nonreciprocity. **c.** At  $T = 12.5$  K, SHG signals appear already at magnetic fields as small as  $\pm 0.03$  T when the antiferromagnetic domains disappear. Further increase of the field shows that each SHG line demonstrates a specific nonreciprocity as a function of the field.

field should be reflected in the SHG field dependences. Figure 3b shows such field dependences of the SHG intensity for several lines at  $T = 4.0$  K, where each line demonstrates its particular dependence. When  $\text{CuB}_2\text{O}_4$  is in the incommensurate phase area marked by arrows between  $-1.67 < B < 1.75$  T in Fig. 3b, no SHG signals are detected. This observation confirms that rotation of the antiferromagnetic vector  $\mathbf{L}$  in the  $(xy)$ -plane, while propagating along the  $z$  axis [26], results in such averaging of its SHG contribution when no signal is observed. Put in other words, the incommensurability destroys the nonreciprocity despite the applied magnetic field. The SHG signal jumps from zero to finite values only after the phase boundary between the incommensurate and commensurate phases is crossed (see Fig. 3a). The different values of the corresponding positive and negative critical fields are characteristic for the first order phase transition. Further field increase leads to gradual rotation of the antiferromagnetic vector  $\mathbf{L}$  in the  $(xy)$  plane, resulting in strong SHG intensity changes as discussed above.

Field dependences of the SHG lines at  $T = 12.5$  K are shown in Fig. 3c. They are drastically different from the corresponding dependences at  $T = 4.0$  K (Fig. 3b). First of all, the SHG intensity decreases by about a factor of ten (compare the intensity scales in both Figures). In contrast to Fig. 3b, the “dead zone” of zero SHG intensity and nonreciprocity is fully suppressed and SHG signals are observed in fields larger than  $\pm 0.03$  T when the antiferromagnetic domains disappear. The SHG field dependences are strongly nonreciprocal and each particular line demonstrates different behavior. Pronounced changes of the rotational anisotropies with temperature are observed when comparing Figs. 2f and 2g.

The entirety of spectral, magnetic field and rotational

anisotropy results at  $T = 4.0$  and 12.5 K in the chosen experimental geometry ( $\mathbf{k} \parallel y$  and  $\mathbf{B} \parallel x$ ) provides unambiguous evidences of SHG nonreciprocity, when  $\text{CuB}_2\text{O}_4$  is in the antiferromagnetic commensurate phase.

#### Voigt geometry $\mathbf{B} \parallel z, \mathbf{k} \parallel y$

We now discuss SHG results for the same  $(xz)$ -plane sample at  $T = 12.5$  K, also for  $\mathbf{k} \parallel y$  in the Voigt geometry, but for the magnetic field  $B = \pm 5$  T applied along the  $z$  axis (Fig. 4a) where  $\text{CuB}_2\text{O}_4$  is in the commensurate phase (Fig. 3a). The strongest SHG signal (Fig. 4b) is observed for the polarizations of the incident light  $\mathbf{E}^\omega \parallel z$  and the SHG light  $\mathbf{E}^{2\omega} \parallel x$ , similar to Fig. 2e. The X1 and X2 peaks in Fig. 4b can be assigned to the two Davydov components [27] similar to Figs. 2d and 2e. As noted above, the crystallographic contribution vanishes at normal incidence  $\mathbf{k} \parallel y$  and therefore the SHG spectra in Fig. 4b definitely have to be assigned to the antiferromagnetic order. In contrast to the  $\mathbf{B} \parallel x$  geometry no field dependence is observed above the saturation field (Fig. 4c). The role of the magnetic field in this case is just to reach saturation of the antiferromagnetic polarization.

In striking contrast to the  $\mathbf{B} \parallel x$  results in Fig. 2, where the SHG nonreciprocity for opposite field directions reaches values as high as 100%, the SHG spectra in Fig. 4b are exactly the same for opposite fields and no nonreciprocity is observed. Moreover, no difference is found in the rotational anisotropies for positive and negative fields of  $B = \pm 5$  T. These results are unambiguously explained on the basis of the detailed symmetry analysis presented in the Supplementary Section S2. In the given geometry at normal incidence, when  $\mathbf{k} \parallel y$ ,

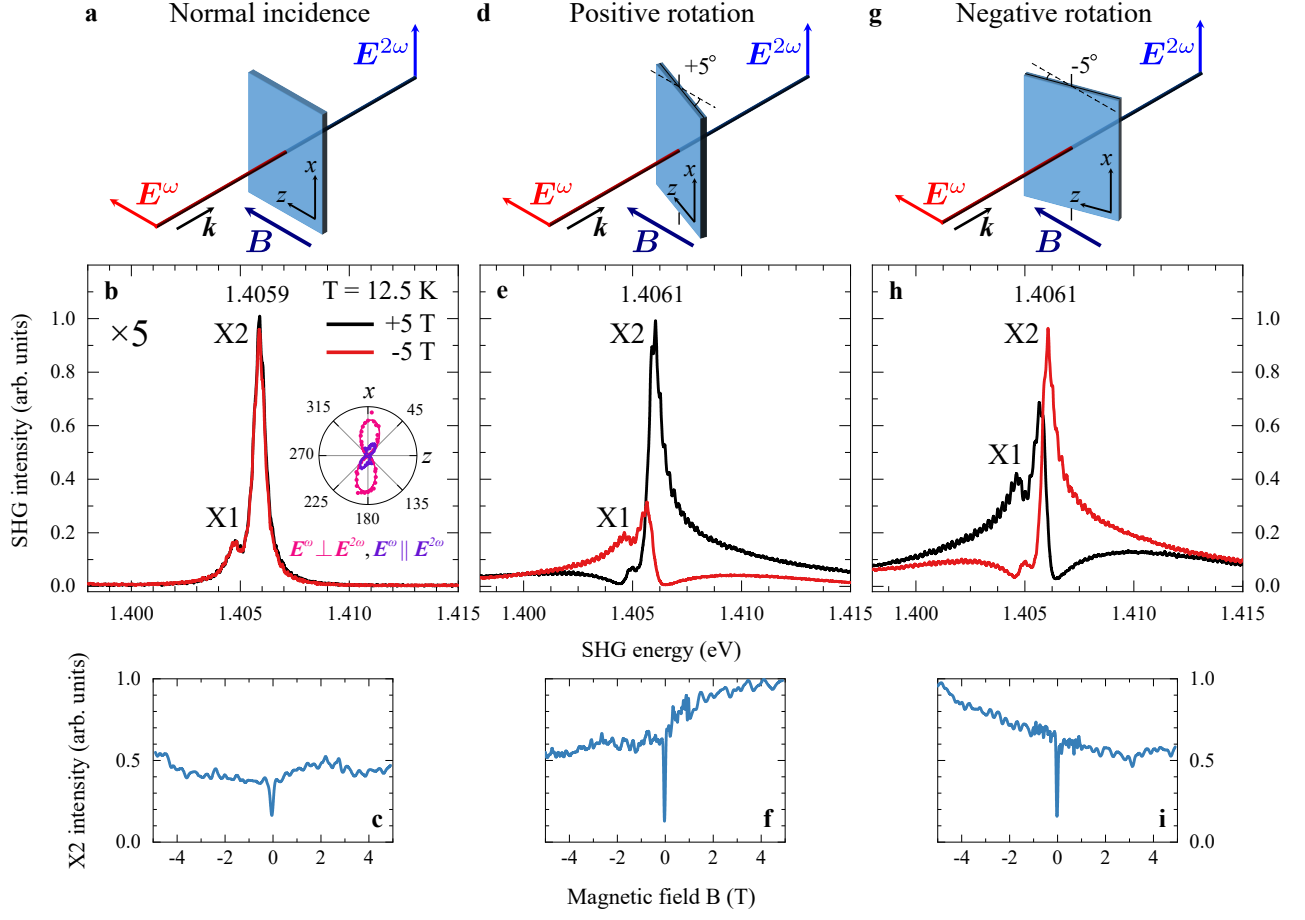


FIG. 4. SHG spectra of  $\text{CuB}_2\text{O}_4$  at normal incidence and for the sample rotated left and right around the  $x$  axis. **a.** Reciprocal SHG spectrum measured at normal incidence for the fundamental light propagating along the  $y$  axis,  $\mathbf{k} \parallel y$ , for the magnetic field  $B = \pm 5$  T in the Voigt geometry,  $\mathbf{B} \parallel z$ . Inset shows SHG rotational anisotropy of the X2 peak for  $\mathbf{E}^\omega \perp \mathbf{E}^{2\omega}$  (red symbols) and  $\mathbf{E}^\omega \parallel \mathbf{E}^{2\omega}$  (black symbols). The rotational anisotropies for the X1 peak are similar to those of the X2 peak (not shown), in contrast to the  $\mathbf{B} \parallel x$  geometry where the two groups showed different behavior (see Fig. 2). Figure 4c shows the SHG intensity as a function of magnetic field, demonstrating saturation in a field as small as  $\sim 50$  mT. A small signal in zero field is explained by incomplete compensation of opposite antiferromagnetic domains. **b.** SHG spectra for the sample rotated around the  $x$  axis by  $5^\circ$  angle. The resulting rotation enables crystallographic SHG contributions and increases the SHG signal by about a factor about five in comparison to Fig. 4a. The interference between resonant and non-resonant contributions results in nonreciprocal Fano-type SHG spectra differing for opposite magnetic fields. **c.** Same as **b.** but for the opposite rotation direction.

$\mathbf{B} \parallel z$ ,  $\mathbf{E}^\omega \parallel z$ , and  $\mathbf{E}^{2\omega} \parallel x$ , the SHG signal can be only induced due to the antiferromagnetic order because  $P_x^{2\omega} = C_{xzz}^L E_z^\omega E_z^\omega L_y$ . Thus, no interference and no non-reciprocity are allowed since the other contributions to the SHG are symmetry-forbidden. The comparison between the  $\mathbf{B} \parallel x$  and  $\mathbf{B} \parallel z$  geometries demonstrates that the antiferromagnetic  $\mathbf{L}$  contribution to the SHG is observed in both cases. However, it is nonreciprocal in the former case when the SHG sign and value are field-dependent (Figs. 2 and 3) and reciprocal in the latter case when they are field-independent (Figs. 4b and 4c).

The magnetoinduced and crystallographic SHG contributions, forbidden at normal incidence, become allowed for oblique incidence when the incident/SHG wave vector  $\mathbf{k}$  does not coincide with any of the crystallographic  $x$ ,  $y$ ,

or  $z$  axes. In fact, when the sample in the  $\mathbf{k} \parallel y$  geometry is slightly rotated in positive (Fig. 4d) or negative (Fig. 4g) direction around the  $x$  axis, the electric field  $\mathbf{E}^\omega$  of the incident wave acquires nonzero projections on the two crystallographic axes ( $E_y^\omega \neq 0$ ,  $E_z^\omega \neq 0$ ) and the nonlinear polarization  $P_x^{2\omega}$  assumes the following form

$$P_x^{2\omega} = C_{xzz}^L E_z^\omega E_z^\omega L_y + 2C_{xyzz}^B E_y^\omega E_z^\omega B_z + 2C_{xyz} E_y^\omega E_z^\omega. \quad (2)$$

Obviously, oblique incidence enables nonreciprocal SHG due to the interference between the antiferromagnetic, magnetoinduced and crystallographic terms in Eq. (2). In the presence of interference, the absolute value of the SHG can be controlled either by inverting the applied magnetic field,  $|P_x^{2\omega}(B_z)| \neq |P_x^{2\omega}(-B_z)|$ , or by invert-

ing the rotation angle, which changes the sign of  $E_y$ ,  $|P_x^{2\omega}(E_y)| \neq |P_x^{2\omega}(-E_y)|$ .

These symmetry arguments are in full agreement with the results presented in Figs. 4e and 4f for positive sample rotation, and in Figs. 4h and 4i for negative rotation. The SHG spectroscopic response changes dramatically when the sample is rotated by only the small angle of about  $\pm 5^\circ$  around the  $x$  axis while keeping unchanged the incident and SHG light propagation direction and the magnetic field  $\mathbf{B} \perp \mathbf{k}$ . The overall increase of the SHG intensity by about a factor of five for the rotated sample (compare Fig. 4b and Figs. 4e,h) is a clear evidence of the crystallographic SHG source becoming activated. It is in agreement with Eq. (2) and manifested by the resonant and non-resonant (extended over a broad spectral range) contributions to the SHG that are independent on the magnetic field. As a result, in the rotated samples the field-dependent and field-independent SHG contributions can interfere and the interference term varies strongly with the applied field. Figs. 4f and 4i show that positive and negative rotations result in opposite magnetic field dependences of the SHG. We note that the rotational anisotropies for the both sample rotations remain similar to that for normal incidence.

The observed asymmetric shapes of the SHG spectra in the rotated samples (Figs. 4f and 4i) resemble a Fano-type resonance [33–35] which, however, is inverted for positive compared to negative sample rotation. Such Fano-shapes arise from the interference of the spectrally broad crystallographic SHG with the resonant SHG induced by the toroidal vector and magnetic field. The inversion of the asymmetry sign for opposite magnetic fields is a direct evidence of the magnetic nonreciprocity.

Symmetry analysis shows that there are three main electric-dipole SHG sources, namely the crystallographic  $C$  source, magnetoinduced  $B$  source, and antiferromagnetic  $L$  source which are shown schematically in Fig. 1c. However, above the antiferromagnetic phase transition at  $T_N = 20$  K the antiferromagnetic  $L$  source vanishes. Nevertheless, two other  $C$  and  $B$  sources in Eq. (2) remain allowed above the transition, and this challenged us to check whether they are capable to lead to the SHG nonreciprocity. Such experiments were carried out and they confirmed that above  $T_N$  at 25 K there is a well-pronounced nonreciprocity due to the interference of crystalline and magnetoinduced contributions. Results are presented and discussed in the Supplementary Section S4B.

To conclude, we have demonstrated a new mechanism of nonlinear nonreciprocity due to the interference of second-harmonic sources induced by the applied magnetic field and the toroidal moment. Moreover, this mechanism of nonreciprocity is supplemented by interference of the toroidal moment with the crystallographic SHG source. In the paramagnetic phase above  $T_N$ , the nonlinear nonreciprocity is observed due to the crystallographic and magnetoinduced contributions to SHG. Our studies showed that  $\text{CuB}_2\text{O}_4$  is a very favorable platform

to explore different sides of resonant nonlinear nonreciprocity induced by a nontrivial spin order. Without any doubt such approach can be generalized to many other antiferromagnets. Nonreciprocal effects, both linear and nonlinear, are of prime importance as efficient tools for studying electronic and magnetic structures of materials as well as for constructing technologically novel nonreciprocal optical and microwave devices. We may add that our result will open new nonlinear degrees of freedom in the emerging field of antiferromagnetic spintronics and opto-spintronics [36–39].

## AUTHOR CONTRIBUTIONS

J.M. performed the experiments and analyzed the data. A.N.P. developed the theoretical model. R.M.D. derived equations and performed calculations of SHG rotational anisotropies. D.R.Y., M.B. and R.V.P. conceived the idea for the experiment. All authors discussed the results and commented on the manuscript. R.V.P. supervised the project.

## COMPETING INTERESTS

The authors declare no competing interests.

## METHODS

For solving the task of registration and distinguishing different nonreciprocal contributions to the SHG processes we used a spectroscopic technique based on application of femtosecond laser pulses at 30 kHz repetition rate. This technique provides high sensitivity and high spectral resolution, limited only by the spectrometer for dispersing the signal. The experimental setup is described in detail in Supplementary Section S1. The method was applied for the SHG study of  $\text{CuB}_2\text{O}_4$  ( $xz$ )-plane single-crystal samples with the incident and SHG light propagating along the  $y$  axis,  $\mathbf{k} \parallel y$ . The covered temperature range 1.9–25 K includes several phase transitions between commensurate and incommensurate antiferromagnetic spin structures, as well as the antiferromagnetic–paramagnetic phase transition at  $T_N = 20$  K [28]. The magnetic field  $\mathbf{B}$  up to  $\pm 10$  T was applied along the main crystallographic  $x$  and  $z$  axes in the Voigt geometry,  $\mathbf{k} \perp \mathbf{B}$ . Rotational anisotropies of the SHG signal were measured for crossed  $\mathbf{E}^\omega \perp \mathbf{E}^{2\omega}$  and parallel  $\mathbf{E}^\omega \parallel \mathbf{E}^{2\omega}$  polarizations of the incident and SHG light. That allowed us to distinguish the symmetry-different contributions to the SHG intensity. The anisotropies were fitted using appropriate equations, derived on the basis of the crystallographic and magnetic symmetry of  $\text{CuB}_2\text{O}_4$  as described in the Supplementary Section S3.

## ACKNOWLEDGEMENTS

We are grateful to M.A. Gorlach and E.L. Ivchenko for useful discussions. The samples used in our study were prepared from single crystals grown by

L.N. Bezmaternykh. We acknowledge the financial support by the Deutsche Forschungsgemeinschaft through the International Collaborative Research Centre 160. A.N.P. acknowledges the partial financial support from the Russian Foundation for Basic Research Grant No.19-52-12038-NNIO\_a. R.V.P. acknowledges the partial financial support by the RFBR Project No.19-52-12063.

- 
- [1] C. Caloz, A. Alù, S. Tretyakov, D. Sounas, K. Achouri, and Z.-L. Deck-Léger, Electromagnetic nonreciprocity, *Phys. Rev. Applied* **10**, 047001 (2018).
- [2] R. J. Potton, Reciprocity in optics, *Rep. Prog. Phys.* **67**, 717 (2004).
- [3] A. K. Zvezdin and V. A. Kotov, *Modern Magneto-optics and Magneto-optical Materials* (Institute of Physics Publishing, Bristol and Philadelphia, 1997).
- [4] Y. Shen, *The Principles of Nonlinear Optics* (Wiley, Hoboken, 2002).
- [5] R. W. Boyd, *Nonlinear Optics* (Academic Press, New York, 2008).
- [6] S. Toyoda, N. Abe, and T. Arima, Nonreciprocal refraction of light in a magnetoelectric material, *Phys. Rev. Lett.* **123**, 077401 (2019).
- [7] Y. Ogawa, Y. Kaneko, J. He, X. Yu, T. Arima, and Y. Tokura, Magnetization-Induced Second Harmonic Generation in a Polar Ferromagnet, *Phys. Rev. Lett.* **92**, 047401 (2004).
- [8] N. A. Spaldin, M. Fiebig, and M. Mostovoy, The toroidal moment in condensed-matter physics and its relation to the magnetoelectric effect, *J. Phys. Condens. Matter* **20**, 434203 (2008).
- [9] M. Fiebig, D. Fröhlich, B. B. Krichevstov, and R. V. Pisarev, Second harmonic generation and magnetic-dipole-electric-dipole interference in antiferromagnetic  $\text{Cr}_2\text{O}_3$ , *Phys. Rev. Lett.* **73**, 2127 (1994).
- [10] M. Fiebig, T. Lottermoser, D. Fröhlich, A. V. Goltsev, and R. V. Pisarev, Observation of coupled magnetic and electric domains, *Nature* **419**, 818 (2002).
- [11] M. Fiebig, V. V. Pavlov, and R. V. Pisarev, Second-harmonic generation as a tool for studying electronic and magnetic structures of crystals, *J. Opt. Soc. Amer. B* **22**, 96 (2005).
- [12] F. Spitzer, A. N. Poddubny, I. A. Akimov, V. F. Sapega, L. Klompaker, L. E. Kreilkamp, L. V. Litvin, R. Jede, G. Karczewski, M. Wiater, T. Wojtowicz, D. R. Yakovlev, and M. Bayer, Routing the emission of a near-surface light source by a magnetic field, *Nat. Phys.* **14**, 1043 (2018).
- [13] Y. Tokura and N. Nagaosa, Nonreciprocal responses from non-centrosymmetric quantum materials, *Nat. Commun.* **9**, 1 (2018).
- [14] S.-W. Cheong, D. Talbayev, V. Kiryukhin, and A. Saxena, Broken symmetries, non-reciprocity, and multiferroicity, *npj Quantum Mater.* **3**, 1 (2018).
- [15] S.-W. Cheong, SOS: symmetry-operational similarity, *npj Quantum Mater.* **4**, 1 (2019).
- [16] V. M. Dubovik and V. V. Tugushev, Toroid moments in electrodynamics and solid-state physics, *Phys. Rep.* **187**, 145 (1990).
- [17] J. Lehmann, C. Donnelly, P. M. Derlet, L. J. Heyderman, and M. Fiebig, Poling of an artificial magneto-toroidal crystal, *Nat. Nanotech.* **14**, 141 (2019).
- [18] B. B. Van Aken, J.-P. Rivera, H. Schmid, and M. Fiebig, Observation of ferrotoroidic domains, *Nature* **449**, 702 (2007).
- [19] C. Ederer and N. A. Spaldin, Towards a microscopic theory of toroidal moments in bulk periodic crystals, *Phys. Rev. B* **76**, 214404 (2007).
- [20] A. S. Zimmermann, D. Meier, and M. Fiebig, Ferroic nature of magnetic toroidal order, *Nat. Commun.* **5**, 1 (2014).
- [21] P. Tolédano, M. Ackermann, L. Bohatý, P. Becker, T. Lorenz, N. Leo, and M. Fiebig, Primary ferrotoroidicity in antiferromagnets, *Phys. Rev. B* **92**, 094431 (2015).
- [22] P. Toledano, D. D. Khalyavin, and L. C. Chapon, Spontaneous toroidal moment and field-induced magnetotoroidic effects in  $\text{Ba}_2\text{CoGe}_2\text{O}_7$ , *Phys. Rev. B* **84**, 094421 (2011).
- [23] A. E. Miroshnichenko, A. B. Evlyukhin, Y. F. Yu, R. M. Bakker, A. Chipouline, A. I. Kuznetsov, B. Lukyanchuk, B. N. Chichkov, and Y. S. Kivshar, Nonradiating anapole modes in dielectric nanoparticles, *Nat. Commun.* **6**, 1 (2015).
- [24] M. Martinez-Ripoll, S. Martinez-Carrera, and S. Garcia-Blanco, The crystal structure of copper metaborate,  $\text{CuB}_2\text{O}_4$ , *Acta Crystallogr. Sect. B* **27**, 677 (1971).
- [25] R. V. Pisarev, I. Sängner, G. A. Petrakovskii, and M. Fiebig, Magnetic-Field Induced Second Harmonic Generation in  $\text{CuB}_2\text{O}_4$ , *Phys. Rev. Lett.* **93**, 037204 (2004).
- [26] M. Boehm, B. Roessli, J. Schefer, A. Wills, B. Oulad-diaf, E. Lelievre-Berna, U. Staub, and G. A. Petrakovskii, Complex magnetic ground state of  $\text{CuB}_2\text{O}_4$ , *Phys. Rev. B* **68**, 024405 (2003).
- [27] K. N. Boldyrev, R. V. Pisarev, L. N. Bezmaternykh, and M. N. Popova, Antiferromagnetic Dichroism in a Complex Multisublattice Magnetoelectric  $\text{CuB}_2\text{O}_4$ , *Phys. Rev. Lett.* **114**, 247210 (2015).
- [28] A. E. Petrova and A. I. Pankrats, Copper metaborate  $\text{CuB}_2\text{O}_4$  phase diagrams based on the results of measuring the magnetic moment, *J. Exp. Theor. Phys.* **126**, 506 (2018).
- [29] M. Fiebig, I. Sängner, and R. V. Pisarev, Magnetic phase diagram of  $\text{CuB}_2\text{O}_4$ , *J. Appl. Phys.* **93**, 6960 (2003).
- [30] S. N. Martynov and A. D. Balaev, Frustration mechanism of formation of a helical magnetic structure in the  $\text{CuB}_2\text{O}_4$  two-subsystem antiferromagnet, *JETP Lett.* **85**, 649 (2007).
- [31] Y. Kousaka, S. Yano, J. Kishine, Y. Yoshida, K. Inoue, K. Kikuchi, and J. Akimitsu, Chiral magnetic ordering and commensurate-to-incommensurate transition

- in  $\text{CuB}_2\text{O}_4$ , *J. Phys. Soc. Jpn.* **76**, 123709 (2007).
- [32] T. Kawamata, N. Sugawara, S. M. Haidar, T. Adachi, T. Noji, K. Kudo, N. Kobayashi, Y. Fujii, H. Kikuchi, M. Chiba, *et al.*, Thermal conductivity and magnetic phase diagram of  $\text{CuB}_2\text{O}_4$ , *J. Phys. Soc. Jpn.* **88**, 114708 (2019).
- [33] U. Fano, Effects of configuration interaction on intensities and phase shifts, *Phys. Rev.* **124**, 1866 (1961).
- [34] A. E. Miroshnichenko, S. Flach, and Y. S. Kivshar, Fano resonances in nanoscale structures, *Rev. Mod. Phys.* **82**, 2257 (2010).
- [35] M. F. Limonov, M. V. Rybin, A. N. Poddubny, and Y. S. Kivshar, Fano resonances in photonics, *Nat. Photon.* **11**, 543 (2017).
- [36] V. Baltz, A. Manchon, M. Tsoi, T. Moriyama, T. Ono, and Y. Tserkovnyak, Antiferromagnetic spintronics, *Rev. Mod. Phys.* **90**, 015005 (2018).
- [37] T. Jungwirth, X. Marti, P. Wadley, and J. Wunderlich, Antiferromagnetic spintronics, *Nat. Nanotech.* **11**, 231 (2016).
- [38] P. Němec, M. Fiebig, T. Kampfrath, and A. V. Kimel, Antiferromagnetic opto-spintronics, *Nat. Phys.* **14**, 229 (2018).
- [39] E. V. Gomonay and V. M. Loktev, Spintronics of antiferromagnetic systems, *Low Temp. Phys.* **40**, 17 (2014).



## Supplementary Information:

### Magneto-toroidal nonreciprocity of second harmonic generation

J. Mund,<sup>1</sup> D. R. Yakovlev,<sup>1,2</sup> A. N. Poddubny,<sup>2</sup>

R. M. Dubrovin,<sup>2</sup> M. Bayer,<sup>1,2</sup> and R. V. Pisarev<sup>2,\*</sup>

<sup>1</sup>*Experimentelle Physik 2, Technische Universität Dortmund, D-44221 Dortmund, Germany*

<sup>2</sup>*Ioffe Institute, Russian Academy of Sciences, 194021 St.-Petersburg, Russia*

#### S1. Experimental setup

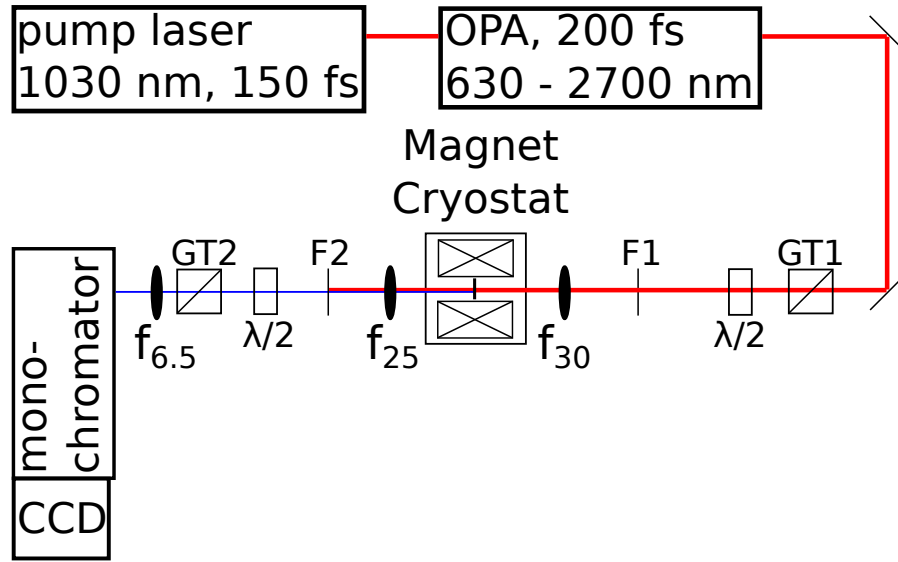


FIG. S1. **Experimental setup.** A schematic representation of the experimental setup for SHG spectroscopy. Optical parametric amplifier (OPA), Glan Thompson linear polarizer (GT), half-wave plate ( $\lambda/2$ ), color filter (F), lens with  $xx$ -cm focal length ( $f_{xx}$ ).

The experimental setup is shown in Fig. S1. The exciting laser (Light Conversion) consists of an optical parametric amplifier (OPA, Orpheus) pumped by a pulsed laser (Pharos). The OPA can be tuned in the spectral range of interest, supplying pulses of about 200 fs duration with a full width at half maximum (FWHM) of 10 meV. The energy per pulse can be up to  $1 \mu\text{J}$  at a repetition rate of 30 kHz. The laser radiation with frequency  $\omega$  and wave vector

$\mathbf{k}^\omega$  hits the sample normal to its surface and is focused there into a spot of about  $100\ \mu\text{m}$  diameter.

With the Glan Thompson polarizer GT1 and the half-wave plates  $\lambda/2$ , the linear polarization of the incoming and outgoing light can be varied continuously and independently around the optical axis. One can thus measure for any fixed polarization of  $\mathbf{E}^\omega$  or  $\mathbf{E}^{2\omega}$  the angular dependence of the other polarization. Of special interest are the rotational anisotropies of the SHG signals for either parallel ( $\mathbf{E}^\omega \parallel \mathbf{E}^{2\omega}$ ) or crossed ( $\mathbf{E}^\omega \perp \mathbf{E}^{2\omega}$ ) polarizations of the laser and the SHG. The GT2 polarizer is set to the optimal polarization of the monochromator, providing highest throughput. The long pass filter F1 prevents SHG from optical elements to enter the monochromator and the short pass filter F2 cuts off the infrared pump light.

The detection of the SHG signal with frequency  $2\omega$  and wave vector  $\mathbf{k}^{2\omega} = 2\mathbf{k}^\omega$  is done by a 0.5-meter monochromator (Acton, Roper Scientific) with a 1800 grooves/mm grating in combination with a Si charge-coupled device (CCD) camera (matrix with  $1340 \times 400$  pixels, pixel size  $20\ \mu\text{m}$ ) cooled by liquid nitrogen. The overall spectral resolution of the detection system at photon energies of 2.8 eV is about  $90\ \mu\text{eV}$ .

For measurements in a magnetic field, a split-coil magnet (Oxford Instruments) is used allowing field strength up to 10 T in the Voigt configuration.

## S2. Symmetry analysis for the second harmonic generation

Here we present a symmetry analysis of the second harmonic generation in  $\text{CuB}_2\text{O}_4$ . Our approach is based on the analysis of the magnetic symmetry of spin ordering in the  $4b$  subsystem performed in Ref. [S1].

### A. Crystallographic symmetry

Crystal symmetry of  $\text{CuB}_2\text{O}_4$  is described by the  $I\bar{4}2m(D_{2d}^{12})$  group [S2; S3]. The corresponding point group  $D_{2d}$  has five classes, including identity operation  $e$ ,  $C_2$  rotation around the tetragonal axis  $z \parallel c$ ,  $S_4$  and  $S_4^3$  improper rotations around  $c$ , two  $C_2'$  rotations around the  $x \parallel a$  and  $y \parallel c$  axes and two  $\sigma_d$  mirror reflections in the planes  $x \pm y$  [S4]. The  $\text{Cu}^{2+}$  ions occupy the  $4b$  Wyckoff positions in the unit cell. They form two equivalent body-centered

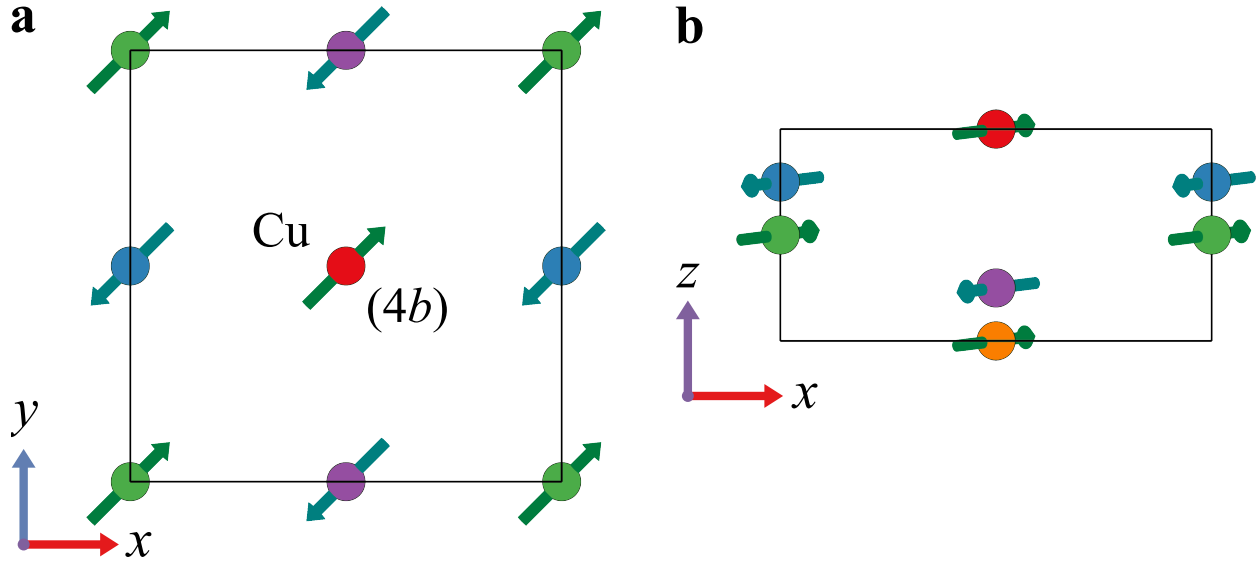


FIG. S2. Projection of CuB<sub>2</sub>O<sub>4</sub> magnetic structure on  $(xy)$  plane (a) and  $(xz)$  plane (b).

sublattices  $4b(A_1)$  and  $4b(A_2)$ , centered at  $(0, 0, c/2)$  and  $(a/2, 0, c/4)$ , as shown in Fig. S2.

In our experiments no SHG signals were observed in the incommensurate phase ( $T > 20$  K) and we will perform analysis only in the commensurate phase, when the magnetic unit cell has the same period as the crystal unit cell. In this case the only relevant difference between the full nonsymmorphic spatial group  $D_{2d}^{12}$  and the point group  $D_{2d}$  is that the operations  $\sigma_d$  and  $C_{2'}$  are accompanied by the nontrivial translations by the vector  $(a/2, 0, 3c/4)$ , respectively. Thus, these operations move Cu<sup>2+</sup> ions from the one  $A$  sublattice to another. All other symmetry operations keep  $4b$  Cu<sup>2+</sup> ions in the same  $A$  sublattice.

The  $D_{2d}$  group has five irreducible representations. Their basis functions, multiplication table and irreducible representations are presented for convenience in Table I.

### B. Selection rules for SHG generation

We are interested in the behavior of the incident (pump) electric field  $\mathbf{E}^\omega$ , second harmonic polarization  $\mathbf{P}^{2\omega}$ , magnetic field  $\mathbf{B}$  and the antiferromagnetic moment  $\mathbf{L} = \mathbf{S}_{A1} - \mathbf{S}_{A2} \perp z$  under the crystal symmetry operations. The components of these vectors, perpendicular to the tetragonal  $c$  axis, transform according to the  $E \equiv \Gamma_5$  irreducible representation. However, specific expressions for the basis functions are different for different vectors: functions  $E_x^\omega, P_x^{2\omega}, B_x, L_y$  transform in the same way as  $x$ , while the functions

TABLE I. Multiplication table for the irreducible representations for the  $D_{2d}$  point group. Functions  $x, y, z$  correspond to Cartesian projections of the polar vector; vector  $\mathbf{B}$  is an axial vector (e.g. magnetic field); vector  $\mathbf{L} = \mathbf{S}_{A1} - \mathbf{S}_{A2}$  describes the antiferromagnetic moment of  $\text{Cu}^{2+}$  (4b) ions [S1].

	$A_1$	$A_2$	$B_1$	$B_2$	$E$
$A_1 \equiv \Gamma_1, x^2 + y^2 \text{ or } z^2$	$A_1$	$A_2$	$B_1$	$B_2$	$E$
$A_2 \equiv \Gamma_2, B_z$		$A_1$	$B_2$	$B_1$	$E; x \propto B_z y, y \propto -B_z x$
$B_1 \equiv \Gamma_3, x^2 - y^2$			$A_1$	$A_2$	$E; x \propto x(x^2 - y^2), y \propto y(y^2 - x^2)$
$B_2 \equiv \Gamma_4, 2xy \text{ or } z$				$A_1$	$E; x \propto yz, y \propto xz$
$E \equiv \Gamma_5, (x, y) \text{ or } (xz, yz) \text{ or } (B_x, -B_y) \text{ or } (L_y, L_x)$					$A_1: x_1x_2 + y_1y_2$ $A_2: x_1y_2 - y_1x_2 \equiv [\mathbf{r}_1 \times \mathbf{r}_2]_z$ $B_1: x_1x_2 - y_1y_2$ $B_2: x_1y_2 + x_2y_1$

$E_y^\omega, P_y^{2\omega}, -B_y, L_x$  transform in the same way as  $y$ . Hence, the symmetry properties of the antiferromagnetic moment  $\mathbf{L}$  are different from both those of the polar vector  $\mathbf{E}^\omega$  and the axial vector  $\mathbf{B}$ , see also the following subsection C for more details. The components of electric field  $E_z^\omega, P_z^{2\omega}$  and magnetic field  $B_z$  along the tetragonal axis are transformed according to the one-dimensional irreducible representations  $B_2 \equiv \Gamma_4$  and  $A_2 \equiv \Gamma_2$ , respectively.

In order to derive the selection rules for the second harmonic (SH) operations we use the multiplication Table I to determine the symmetry properties of the products of type  $E_\alpha E_\beta$  for crystallographic SHG,  $E_\alpha E_\beta L_\gamma$  for the antiferromagnetic SHG and the  $E_\alpha E_\beta B_\gamma$  for the magnetoinduced SHG ( $\alpha, \beta, \gamma = x, y, z$ ). According to the Wigner-Eckart theorem [S4], we need to find the symmetrized products that transform in the same way as the SH polarization  $\mathbf{P}^{2\omega}$ .

We start the analysis from the crystallographic SHG. According to Table I, the functions  $E_x^\omega E_z^\omega$  and  $E_y^\omega E_z^\omega$  transform as the basis functions  $x$  and  $y$  of the irreducible representation  $E$ ; while the product  $E_x^\omega E_y^\omega$  belongs to the irreducible representation  $B_2$ . Hence, these two types of products contribute to the corresponding components of SHG polarization  $P_x, P_y$

and  $P_z$  with different weights  $C_{xyz} = C_{yxz}$  and  $C_{zyx} = C_{zxy}$  :

$$\begin{aligned} P_x^{2\omega} &= 2C_{xyz}E_y^\omega E_z^\omega, \\ P_y^{2\omega} &= 2C_{xyz}E_x^\omega E_z^\omega, \\ P_z^{2\omega} &= 2C_{zyx}E_x^\omega E_y^\omega. \end{aligned} \quad (\text{S1})$$

TABLE II. Multiplication table to derive the selection rules for magnetoinduced and antiferromagnetic SHG. Left column indicate the symmetry properties of the products of electric field components  $E_\alpha^\omega E_\beta^\omega$ . Top row shows the transformation rules for the projections of magnetic field and antiferromagnetic moment  $B_\gamma$  and  $L_\gamma$ . The cells indicate the transformation properties of the products  $E_\alpha E_\beta B_\gamma$  and  $E_\alpha E_\beta L_\gamma$ . Blue color indicates contributions to Eqs. (1) and (2) of the main text.

	$A_2 : B_z$	$E : (B_x, -B_y)$ or $(L_y, L_x)$
$A_1 : E_x^{\omega,2} + E_y^{\omega,2}$	$A_2$	$E : P_x^{2\omega} = (E_x^{\omega,2} + E_y^{\omega,2})(C_{xxxx}^B B_x + C_{xxxy}^L L_y);$ $P_y^{2\omega} = (E_x^{\omega,2} + E_y^{\omega,2})(-C_{xxxx}^B B_y + C_{xxxy}^L L_x)$
$A_1 : E_z^{\omega,2}$	$A_2$	$P_x^{2\omega} = E_z^{\omega,2}(C_{xzzx}^B B_x + C_{xzzx}^L L_y);$ $P_y^{2\omega} = E_z^{\omega,2}(-C_{xzzx}^B B_y + C_{xzzx}^L L_x)$
$B_1 : E_x^{\omega,2} - E_y^{\omega,2}$	$P_z^{2\omega} = C_{zxzx}^B (E_x^{\omega,2} - E_y^{\omega,2}) B_z$	$P_x^{2\omega} = (E_x^{\omega,2} - E_y^{\omega,2})(-C_{yyyx}^B B_y + C_{yyyx}^L L_x);$ $P_y^{2\omega} = -(E_x^{\omega,2} - E_y^{\omega,2})(C_{yyyx}^B B_x + C_{yyyx}^L L_y)$
$B_2 : E_x^\omega E_y^\omega$	$B_1$	$P_x^{2\omega} = 2E_x^\omega E_y^\omega (-C_{yxyx}^B B_y + C_{yxyx}^L L_x);$ $P_y^{2\omega} = 2E_x^\omega E_y^\omega (C_{yxyx}^B B_x + C_{yxyx}^L L_y)$
$E : (E_x^\omega E_z^\omega, E_y^\omega E_z^\omega)$	$P_x^{2\omega} = 2C_{xyzz}^B E_y^\omega E_z^\omega B_z$ $P_y^{2\omega} = -2C_{xyzz}^B E_x^\omega E_z^\omega B_z$	$P_z^{2\omega} = 2E_x^\omega E_z^\omega (-C_{zyzx}^B B_y + C_{zyzx}^L L_x)$ $+ 2E_y^\omega E_z^\omega (C_{zyzx}^B B_x + C_{zyzx}^L L_y)$

Now we proceed to the antiferromagnetic and magnetoinduced SHG. To this end, we first write the transformation products of all the possible products  $E_\alpha^\omega E_\beta^\omega$  of electric field projections in the left column of Table II. Top row of the table lists the projections of magnetic field  $\mathbf{B}$  and antiferromagnetic vector  $\mathbf{L}$ . Next, we fill the cells of the multiplication Table II by the symmetry properties of different possible products  $E_\alpha E_\beta B_\gamma$  and  $E_\alpha E_\beta L_\gamma$  of these projections. The combinations transforming in the same way as  $\mathbf{P}^{2\omega}$  yield the desired selection rules for the SHG. The combinations highlighted by the blue color yield Eq. (2) for the SHG in the main text. We note, that the contributions to the SHG linear in the

ferromagnetic moment  $\mathbf{M} = \mathbf{S}_1 + \mathbf{S}_2$  can also be obtained from the Table II. The reason is that vectors  $\mathbf{B}$  and  $\mathbf{M}$  transform in the same way, so the symmetry of the corresponding tensor  $C_{ijkl}^M$  is the same as for  $C_{ijkl}^B$ .

### C. Antiferromagnetic contribution to the SHG and its relation to the toroidal moment

In this section we analyze in more detail the contribution to the SHG, linear in antiferromagnetic moment  $\mathbf{L}$ . It is described by the tensor components  $C_{xzz y}^L = C_{yzz x}^L$ , or, explicitly,

$$P_x^{2\omega} = C_{xzz y}^L E_z^{\omega,2} L_y, \quad P_y^{2\omega} = C_{xzz y}^L E_z^{\omega,2} L_x. \quad (\text{S2})$$

Since the intensity of light along the tetragonal axis  $E_z^{\omega,2}$  is an invariant in the group  $D_{2d}^{12}$ , Eq. (S2) follows directly from the basis functions of the representation  $\Gamma_5 \equiv E$ , i.e.  $P_x^{2\omega}$  transforms in the same way as  $L_y$  and  $P_y^{2\omega}$  transforms in the same way as  $L_x$ . Our goal is to get better understanding of this linear relation between the SHG and the antiferromagnetic vector. It is instructive to link the vector

$$\mathbf{T} = L_y \hat{\mathbf{x}} + L_x \hat{\mathbf{y}} \quad (\text{S3})$$

to the toroidal vector [S5]

$$\mathbf{T} = \frac{1}{2} \sum_j \mathbf{r}_j \times \mathbf{S}_j. \quad (\text{S4})$$

The toroidal moment Eq. (S4) behaves as a vector, and hence the effects proportional to  $\mathbf{P}^{2\omega} \propto \mathbf{t}$  should be allowed by the point group symmetry. However, it is not fully clear at the moment [S5], how the expression Eq. (S4), written for a localized spin distribution, can be generalized to a periodic crystal. It has been suggested [S6] that the observation of SHG in multiferroic FeGaO<sub>3</sub> is related to the toroidal moment

$$\mathbf{E}^{2\omega} \propto \mathbf{T} = \mathbf{P} \times \mathbf{M}, \quad T_x = P_z M_y, \quad T_y = -P_z M_x, \quad (\text{S5})$$

where  $\mathbf{M}$  is the ferrimagnetic moment (resulting from unbalance between two antiferromagnetically-coupled sublattices) and  $\mathbf{P} \parallel z$  is the electric polarization. However, the symmetry structure of our Eq. (S2) is different from Eq. (S5). The reason is the analysis of toroidal moment in [S6] has been performed for the different crystal structure. Therefore, it is not clear why results for toroidal moment from [S6; S7] should apply to CuB<sub>2</sub>O<sub>4</sub>.

In our case the tensor linking  $\mathbf{P}^{2\omega}$  and  $\mathbf{L}$  is symmetric, while in Eq. (S5) this tensor is antisymmetric. We explain this difference by the nonsymmorphic nature of the symmetry group  $D_{2d}^{12}$  of  $\text{CuB}_2\text{O}_4$ . For a better understanding of Eq. (S2) we write the spin density in the antiferromagnetic phase as

$$\mathbf{l}(\mathbf{r}) = P_z(\mathbf{r})\mathbf{S}, \quad P_z(\mathbf{r}) = \sum_j [\delta(\mathbf{r} - \mathbf{r}_{A_1,j}) - \delta(\mathbf{r} - \mathbf{r}_{A_2,j})], \quad S_z = 0. \quad (\text{S6})$$

where the summation runs over the  $4b$   $\text{Cu}^{2+}$  ions in sublattices  $A_1$  and  $A_2$ . The symmetry properties of  $\mathbf{l}(\mathbf{r})$  are determined by the product of the representations governing the transformation of  $P_z(\mathbf{r})$  and the spin  $\mathbf{S}$ . The spin components  $S_x$  and  $S_y$  behave under the point symmetry operations as the  $x$  and  $-y$ , respectively, i.e. in the same way as a pseudovector in a  $D_{2d}$  point group [S4]. The function  $P_z(\mathbf{r})$  belongs to the irreducible representation  $\Gamma_2 \equiv A_2$ , i.e. behaves under the symmetry operations as a  $z$ -component of a pseudovector. This follows from the fact that two  $A$  sublattices are linked by the rotations  $C'_2$  and the mirror reflections  $\sigma_d$ , that require nontrivial translation in the  $D_{2d}^{12}$  spatial group. Thus, the  $\sigma_d$  operation swaps the sublattices and changes the sign of  $P_z$ , in the same way changes the sign of a pseudovector component  $B_z$ . According to Table I, the product of the  $A_2$  representations with the basis function  $P_z$  and  $E$  with the basis functions  $X, Y$  is the  $E$  representation with the basis functions  $x \propto -P_z Y$ ,  $y \propto P_z X$ . Substituting  $Y = -S_y$  and  $X = S_x$ , we find that  $P_z S_y \equiv L_y$  transforms as  $x$  and  $P_z S_x \equiv L_x$  transforms as  $y$ . This is in full agreement with Table I and Eq. (S2). To summarize, we find that Eq. (S5) in our system can be formally generalized to

$$\mathbf{E}^{2\omega} \propto \mathbf{T} = L_y \hat{x} + L_x \hat{y} = P_z \otimes \mathbf{S}, \quad (\text{S7})$$

where the vector product is replaced by the direct one. This equation can be seen as a generalization of the toroidal moment Eq. (S5) for the nonsymmorphic  $D_{2d}^{12}$  crystal structure of  $\text{CuB}_2\text{O}_4$ .

#### D. Toroidal and quadrupolar contributions to the linear magnetoelectric effect

It is instructive to analyze the static magnetoelectric effect [S8], where the polarization at zero frequency  $\mathbf{P}$  is proportional to the antiferromagnetic momentum  $\mathbf{L}$  and the applied magnetic field  $\mathbf{B}$ . Using the transformation rules for the vectors  $\mathbf{P}$ ,  $\mathbf{L}$ ,  $\mathbf{B}$ , discussed above

and summarized in the Table I, we find the magnetoelectric relationship in  $\text{CuB}_2\text{O}_4$  in the following form

$$P_j = \alpha_{jk}^{(em)} B_k. \quad (\text{S8})$$

where the magnetoelectric tensor  $\alpha^{(em)}$  reads

$$\alpha^{(em)} = \begin{pmatrix} 0 & 0 & uL_x \\ 0 & 0 & -uL_y \\ vL_x & -vL_y & 0 \end{pmatrix} \quad (\text{S9})$$

and is described by two independent coefficients  $u$  and  $v$ . Following [S5], we separate the magnetoelectric tensor into symmetric and antisymmetric parts and rewrite Eq. (S8) as

$$\mathbf{P} = -\mathbf{t} \times \mathbf{B} + Q\mathbf{B}. \quad (\text{S10})$$

Here the vector

$$\mathbf{t} = \frac{u-v}{2}(\mathbf{e}_x L_y + \mathbf{e}_y L_x), \quad (\text{S11})$$

dual to the antisymmetric part of the tensor  $\alpha^{(em)}$ , is the toroidal moment vector. It is proportional to the toroidal moment vector  $\mathbf{T}$  Eq. (S3), derived in the following subsection in a different fashion. The symmetric part of the antiferromagnetic tensor

$$Q_{jk} = \frac{1}{2}(\alpha_{jk}^{(em)} + \alpha_{kj}^{(em)}) = \frac{u+v}{2} \begin{pmatrix} 0 & 0 & L_x \\ 0 & 0 & -L_y \\ L_x & -L_y & 0 \end{pmatrix} \quad (\text{S12})$$

describes the magnetic quadrupole response. Comparing Eq. (S2) with Eq. (S11) we again confirm that the observed SHG contribution due to antiferromagnetic moment can be written as

$$\mathbf{P}^{2\omega} \propto \mathbf{t}(E_z^\omega)^2, \quad (\text{S13})$$

i.e. it is proportional to the toroidal vector.

### S3. Analytical expressions for rotational anisotropies of SHG

The electric field of incident light  $\mathbf{E}^\omega$  with polarization in  $xz$  plane ( $E_x^\omega, E_z^\omega \neq 0, E_y^\omega = 0$ ) is given by

$$\begin{cases} E_x^\omega = E^\omega \cos \phi, \\ E_z^\omega = E^\omega \sin \phi, \end{cases} \quad (\text{S14})$$





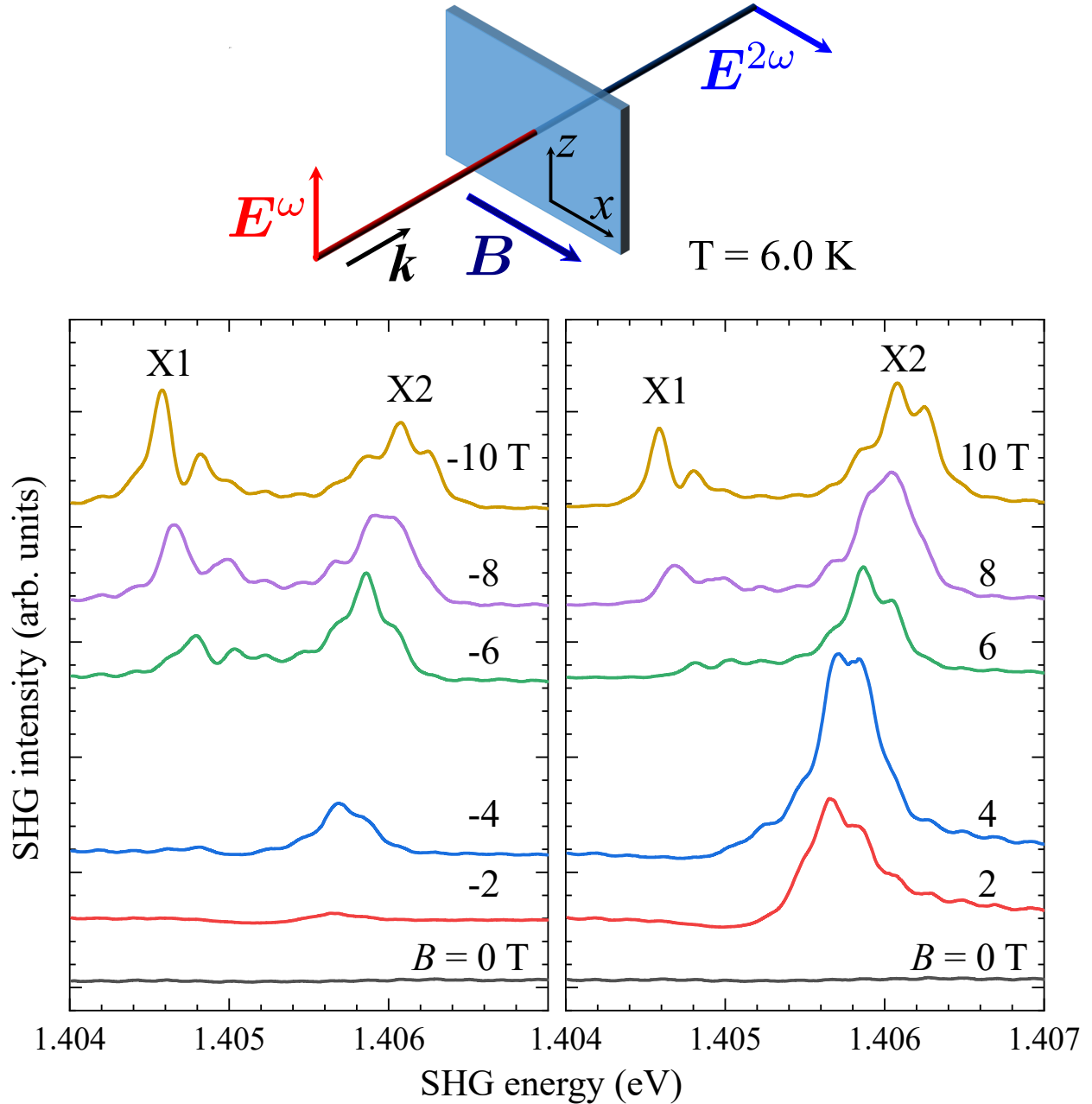


FIG. S3. SHG spectra for  $\pm B$  from 0 to 10 T at  $T=6$  K.

the  $4b$  spin system is in the incommensurate phase in accordance with the phase diagram in Fig. 3a. These spectra confirm complementarity and reliability of the results at  $T=4$  K shown in Fig. 3b. Field increase leads to evolution of the both group of lines marked as X1 and X2 but in different way for the positive and negative field. In the positive field X2 group dominates in the SHG spectra, whereas in the negative field the SHG intensity of X1 group overcomes that of the X2 group. Such complex behaviour of SHG lines is definitely

related to their microscopic nature but such an analysis is outside the scope of this article.

### B. Nonreciprocity of the SHG spectra above $T_N=20$ K

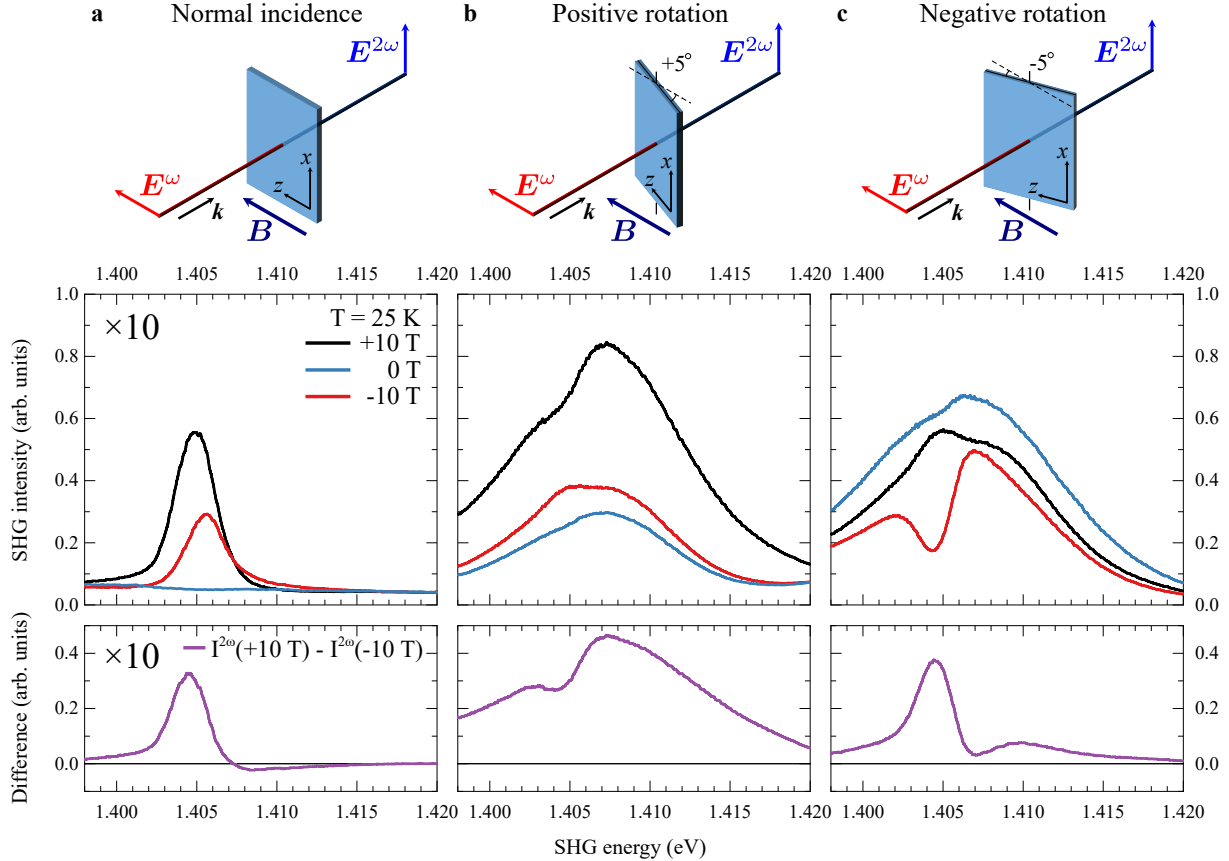


FIG. S4. SHG spectra at  $T=25$  K.

Symmetry analysis shows that in the electric-dipole approximation there are three main SHG sources, namely the  $C$  source related to the noncentrosymmetric crystal structure, the magnetic-field induced  $B$  source, and the antiferromagnetic  $L$  source. All of them are shown schematically in Fig. 1c and in Eq. (2). Their transformation properties are different as shown in Tables I and II presented above in Supplementary Information. It was a challenging task to verify whether the  $C$  and  $B$  sources survive in the paramagnetic phase above  $T_N=20$  K when the antiferromagnetic source  $L$  vanishes.

To solve this challenging task experiments were carried out at  $T=25$  K and results are shown in Fig. S4. Experiments were carried out at normal incidence and with the sample rotated around the  $x$  axis in positive and negative direction similar to results presented in Fig. 2. It

should be noted first of all that a dramatic drop of the SHG intensity above  $T_N$  occurs. In order to register the signal we had to increase by about an order of magnitude the intensity of the incident beam and to perform measurements in the largest available field  $\pm B=10$  T. This allowed us to obtain reliable and convincing results. Fig. S4a shows that at normal incidence when crystallographic contribution is symmetry forbidden there is no SHG signal in zero field. However, reliable signals are observed in magnetic field, which are different for opposite fields demonstrating another side of magnetoinduced SHG nonreciprocity. SHG intensity is strongly increased for the tilted sample due to emergence of crystallographic off-resonant and resonant SHG contributions. The interference between the crystallographic and field-induced SHG is well pronounced in Figs. S4b and S4c, and in particular for the negative-tilted sample.

---

\* pisarev@mail.ioffe.ru

- [S1] M. Boehm, B. Roessli, J. Schefer, A. Wills, B. Ouladdiaf, E. Lelievre-Berna, U. Staub, and G. A. Petrakovskii, Complex magnetic ground state of  $\text{CuB}_2\text{O}_4$ , *Phys. Rev. B* **68**, 024405 (2003).
- [S2] M. Martinez-Ripoll, S. Martinez-Carrera, and S. Garcia-Blanco, The crystal structure of copper metaborate,  $\text{CuB}_2\text{O}_4$ , *Acta Crystallogr. Sect. B* **27**, 677 (1971).
- [S3] M. I. Aroyo, J. M. Perez-Mato, D. Orobengoa, E. M. R. E. Tasci, G. de la Flor, and A. Kirov, Crystallography online: Bilbao crystallographic server, *Bulg. Chem. Commun* **43**, 183 (2011).
- [S4] M. S. Dresselhaus, G. Dresselhaus, and A. Jorio, *Group Theory. Application to the Physics of Condensed Matter* (Springer-Verlag Berlin Heidelberg, 2008, 2008).
- [S5] N. A. Spaldin, M. Fiebig, and M. Mostovoy, The toroidal moment in condensed-matter physics and its relation to the magnetoelectric effect, *J. Phys. Condens. Matter* **20**, 434203 (2008).
- [S6] Y. Tokura and N. Nagaosa, Nonreciprocal responses from non-centrosymmetric quantum materials, *Nat. Commun.* **9**, 1 (2018).
- [S7] S. Toyoda, N. Abe, and T. Arima, Nonreciprocal Refraction of Light in a Magnetoelectric Material, *Phys. Rev. Lett.* **123**, 077401 (2019).
- [S8] I. E. Dzyaloshinskii, On the magneto-electrical effect in antiferromagnets, *Sov. Phys. JETP* **37**, 881 (1959).